

Milling-Induced “Turn-off” Luminescence in Copper Nanoclusters

Subrata Duary, Arijit Jana, Amitabha Das, Swetashree Acharya, Amoghavarsha Ramachandra Kini, Jayoti Roy, Ajay Kumar Poonia, Deepak Kumar Patel, Vivek Yadav, P. K. Sudhadevi Antharjanam, Biswarup Pathak,* Adarsh Kumaran Nair Valsala Devi,* and Thalappil Pradeep*

Cite This: <https://doi.org/10.1021/acs.inorgchem.4c02617>

Read Online

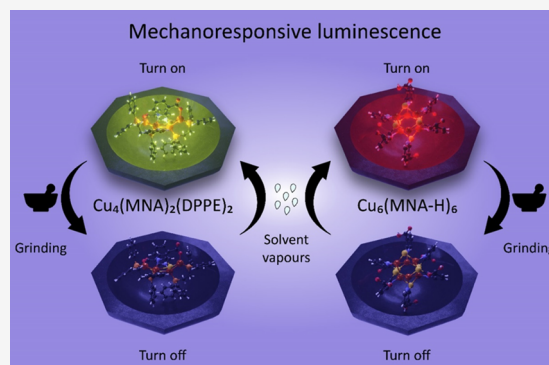
ACCESS |

Metrics & More

Article Recommendations

Supporting Information

ABSTRACT: Atomically precise copper nanoclusters (NCs) attract research interest due to their intense photoluminescence, which enables their applications in photonics, optoelectronics, and sensing. Exploring these properties requires carefully designed clusters with atomic precision and a detailed understanding of their atom-specific luminescence properties. Here, we report two copper NCs, $[\text{Cu}_4(\text{MNA})_2(\text{DPPE})_2]$ and $[\text{Cu}_6(\text{MNA-H})_6]$, shortly Cu_4 and Cu_6 , protected by 2-mercaptonicotinic acid (MNA- H_2) and 1,2-bis(diphenylphosphino)ethane (DPPE), showing “turn-off” mechanoresponsive luminescence. Single-crystal X-ray diffraction reveals that in the Cu_4 cluster, two Cu_2 units are appended with two thiols, forming a flattened boat-shaped Cu_4S_2 kernel, while in the Cu_6 cluster, two Cu_3 units form an adamantane-like Cu_6S_6 kernel. High-resolution electrospray ionization mass spectrometry studies reveal the molecular nature of these clusters. Lifetime decay profiles of the two clusters show the average lifetimes of 0.84 and 1.64 μs , respectively. These thermally stable Cu NCs become nonluminescent upon mechanical milling but regain their emission upon exposure to solvent vapors. Spectroscopic data of the clusters match well with their computed electronic structures. This work expands the collection of thermally stable and mechanoresponsive luminescent coinage metal NCs, enriching the diversity and applications of such materials.



INTRODUCTION

Atomically precise nanoclusters (NCs) are a distinct category of nanomaterials with a core dimension below 3 nm, showing unique physicochemical properties.^{1–5} Such materials have intrinsic molecule-like discrete electronic energy levels with molecular luminescence.^{6–8} Noble metal NCs are protected by thiol, amine, carbene, alkyne, phosphine, and carboxylic acid ligands, which control their size, shape, stability, optoelectronic properties, and chemical reactivity.^{9–14} Extensive investigations of gold and silver NCs have yielded valuable insights into their synthesis, structure, properties, and structure–property relationships.^{15,16} However, complex synthetic procedures, expensive precursors, low synthetic yields, and poor chemical purity are prime drawbacks, limiting the practical utility of several clusters.¹⁷ Alternatively, Cu NCs are promising candidates because Cu is more earth-abundant and less expensive, and there are several nontoxic precursors. Besides, the methods provide high synthetic yields.^{18–22} Recently, many moderate-sized and large Cu clusters, such as Cu_{18} , Cu_{20} , Cu_{29} , Cu_{33} , Cu_{58} , Cu_{62} , Cu_{74} , Cu_{81} , Cu_{93} , Cu_{96} , and Cu_{136} were synthesized, and several single-crystal X-ray structures were determined.^{23–27} Noble metal NCs, composed of gold and silver with specific nuclearity, generally exhibit luminescence with relatively low quantum yields, and their emission lifetimes range from the picosecond to the nanosecond time scale. In

contrast, copper clusters show longer lifetimes of the microsecond time scale and higher quantum yields, which motivated us to investigate their structure–property relationships in greater detail.³⁵

Generally, it has been observed that Cu NCs with low nuclearity exhibit strong, multicolor, and tunable luminescence due to their facile charge transfer between the ligand shell and metal.³⁶ Due to their intense luminescence in small Cu NCs, they may be used in various applications like light-emitting diodes, electroluminescence, anticounterfeiting, cell imaging, and optical sensing.^{28–34} Reports suggest that the involvement of Cu *d* orbitals and metal-to-ligand charge transfer or vice versa is likely to be responsible for their bright luminescence.^{37,38} For example, electron-donating ligands like amines and phosphines induce intense luminescence in ultrasmall Cu clusters.^{18,39} The intensity of emission originating in NCs depends on factors like chemical environment and restriction

Received: June 24, 2024

Revised: September 12, 2024

Accepted: September 17, 2024

of intramolecular motion, controlled by surface ligands.^{40–42} Sometimes, a decrease in the molecular motions in the crystalline state enhances luminescence, popularly known as crystallization-induced emission.^{41,42} This type of intermolecular aggregation occurs due to CH– π and π – π interactions and hydrogen bonding, which together enhance the emission intensity.^{43,44} The bulky surface ligands, such as aromatic thiols, amines, and phosphines, stabilizing the metal–sulfur core in NCs, form a rigid framework, contributing to the chemical and thermal stability of the molecules or their packing in a stable crystalline state. The Cu–S core of a crystalline ordered structure in small Cu NCs is sensitive to external stimuli like temperature, pressure, and radiation.^{35,45–51} Cu NCs with such diverse properties motivated us to synthesize, crystallize, and explore the properties of new clusters for a rational understanding.

Reports of small Cu clusters and complexes with long Cu–Cu bond lengths protected by phosphines show mechanochromic luminescence.^{47–49} This is ascribed to the reversibility of molecular conformations and intermolecular interactions during transitions between thermodynamically stable crystalline and metastable amorphous states.⁵⁰ These transitions in Cu NCs are sometimes accompanied by changes in the excited states, which result in different types of luminescence upon mechanical stimuli.

In the present work, we have synthesized two luminescent Cu NCs, Cu₄ and Cu₆, primarily protected by 2-mercaptocotinic acid (MNA-H₂), following the strategy of ligand-exchange-induced structural transformation (LEIST). Single-crystal X-ray diffraction (SC-XRD) reveals their molecular structures and other spectroscopic studies were used to characterize them thoroughly. The Cu₄ cluster emits green luminescence, whereas Cu₆ emits red in its crystalline state under ambient conditions. Due to reversible phase transformations, these clusters manifest “turn-off” luminescence upon mechanical milling and partial luminescence recovery upon exposure to solvent vapor. Density functional theory (DFT) calculations provide a detailed understanding of their structures and properties. These mechanoresponsive Cu NCs with direct Cu–Cu bonds represent a burgeoning area of research with potential for applications.

EXPERIMENTAL SECTION

Materials and Chemicals. Copper iodide (CuI), 1,2-bis(diphenylphosphino)ethane (DPPE), sodium borohydride (NaBH₄, 98%), and 2-mercaptocotinic acid (MNA-H₂) were purchased from Sigma-Aldrich. Potassium bromide (KBr, IR grade) was obtained from Sigma-Aldrich. Milli-Q water was used for purification. HPLC-grade acetonitrile (ACN), methanol (MeOH), N,N-dimethylformamide (DMF), and dichloromethane (DCM) were purchased from Finar and Rankem Chemicals. All of the reagents and solvents were used as received, without further purification.

Characterization Techniques. Optical absorption spectral measurements were recorded using a PerkinElmer Lambda 365 UV–vis spectrometer with a bandpass filter of 1 nm. A Waters Synapt G2Si high-definition mass spectrometer was used to measure the mass of the NCs. The following conditions—flow rate of 20 μ L/min, capillary voltage of 3 kV, source temperature of 100 °C, desolvation temperature of 150 °C, and gas flow rate of 400 L/h—were optimized for ionization of the NCs in ACN. The photoluminescence spectra were collected using a Jobin Yvon NanoLog fluorescence spectrometer with a bandpass filter of 3 nm for emission and excitation. A HORIBA DeltaFlex time-correlated single-photon counting spectrometer equipped with a detector, HORIBA PPD-850 (HORIBA Delta Diode 405 nm laser), was used to measure the

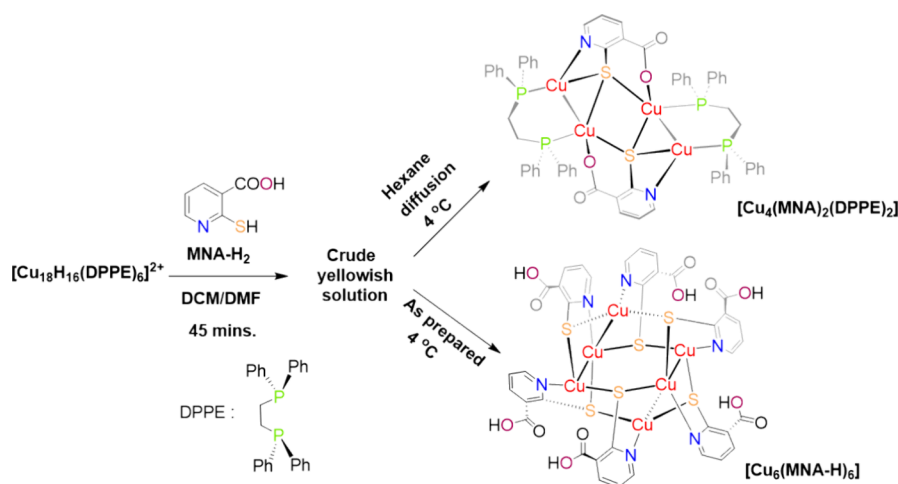
lifetime of the NCs. An FLS 1000 spectrometer with Fluoracel software equipped with a xenon arc lamp was used for photoluminescence quantum efficiency measurements. To calculate radiative and nonradiative decay rate constants (k_r and k_{nr}), the following formula was used, $k_r = \Phi/\tau_{avg}$ and $k_{nr} = 1/\tau_{avg} - \Phi$ (where Φ is the quantum yield and τ_{avg} is the average lifetime). A PerkinElmer FT-IR JASCO-4100 spectrometer was also used (2 mg of sample in 20 mg of dry KBr). X-ray photoelectron spectroscopy (XPS) of NCs was recorded using an ESCA Probe TPD spectrometer of Omicron Nanotechnology, equipped with a polychromatic Mg K α X-ray source ($h\nu = 1253.6$ eV). The binding energy of different elements was calibrated for C 1s (285.0 eV). SCXRD data of single crystals were collected using a Bruker D8 VENTURE instrument, equipped with a Mo K α radiation source (0.71073 Å) and a PHOTON II detector. The structure was solved by SHELXT-2018 and refined by full-matrix least-squares techniques using the SHELXL-2018 software package incorporated in the WinGX system version v2018.3. For molecular-level DFT calculations, the Gaussian 09 D.01 program was used. Powder XRD data of microcrystalline solids were collected using a D8 Advance Bruker instrument with a Cu K α X-ray source of 1.54 Å. Thermogravimetric (TG) analysis, derivative thermogravimetry (DTG), and differential scanning calorimetry measurements of microcrystals were recorded (25–1000 °C, N₂ gas flow 20 mL/min.) using a NETZSCH STA 449 F3 Jupiter instrument equipped with Proteus-6.1.0 software. An optical microscope from LEICA equipped with LAS V4.8 software was used to see the single crystals of NCs at different magnifications and polarization angles. Field-emission scanning electron microscopy (FESEM) images of single crystals and their energy-dispersive X-ray spectroscopy analysis were performed with a Verios G4 UC FEI instrument. Crystals were drop-cast onto the substrate (TEM grid) and dried at room temperature. The sample was sputter-coated with gold (Au) to produce better-quality images.

Synthesis of [Cu₁₈H₁₆(DPPE)₆]²⁺. The Cu₁₈ NC was synthesized following the procedure available in the literature.⁵² In brief, 95 mg of CuI and 120 mg of DPPE were mixed in 13 mL of ACN. The metal ion was then reduced with 180 mg of dry NaBH₄. After 3 h of stirring, an orange precipitate was formed. The residue was washed multiple times with ACN and MeOH. After that, it was dissolved in DCM and used for characterization.

Synthesis of Cu₄ and Cu₆ NCs. The Cu₄ and Cu₆ NCs were synthesized by using a one-pot LEIST method starting from the Cu₁₈ precursor. The purified Cu₁₈ (~35 mg) dissolved in 4 mL of DCM was reacted with 15 mg of 2-mercaptocotinic acid in 1 mL of DMF. Initially, the reaction mixture was transparent and reddish. After 45 min, the solution became yellowish, and the reaction was stopped. Cu₄ was crystallized by hexane vapor diffusion to yield a crude yellowish solution at 4 °C, whereas Cu₆ was crystallized from the crude solution at 4 °C. The yields of Cu₄ and Cu₆ NCs were 75 and 60%, respectively, for the Cu precursor. UV/vis spectra of clusters were measured in acetonitrile.

Photoluminescence Measurement. Photoluminescence spectra of microcrystalline Cu₄ and Cu₆ NCs (around 70–80 mg) were measured. The Cu₄ NC shows green emission (around 560 nm), and the Cu₆ NC shows red emission (around 755 nm). The nature of the excited state of these clusters was verified through O₂ sensitivity PL experiments. Around 25 mg of the solid sample was taken in a glass vial and kept under a vacuum for 1 h. O₂ gas at atmospheric pressure was exposed for 2 h, and the corresponding emission spectrum was measured just after oxygen exposure. Temperature-dependent (ranging from ambient room temperature to 200 °C) photoluminescence spectra of microcrystalline NCs were measured.

Mechanosensitive Luminescence. Mechanical milling and solvent exposure studies were performed to evaluate the mechanoresponsive luminescence. The sample was ground in a mortar and pestle at room temperature. The luminescence of these materials (Cu₄ and Cu₆ NCs) was vanished upon milling, while the luminescence was regained after the diffusion of DCM and DMF vapors. This behavior of clusters was monitored through PL and PXRD measurements. The effect of other solvent vapors was also studied.

Scheme 1. Schematic Representation of the Synthesis of Cu₄ and Cu₆ Clusters Following the LEIST Method and Their Crystallization

RESULTS AND DISCUSSION

Synthesis and Characterization. The Cu₄(MNA)₂(DPPE)₂ and Cu₆(MNA-H)₆ clusters (Cu₄ and Cu₆ subsequently) were synthesized under ambient conditions, following the LEIST reaction in a DCM and DMF (4:1, v/v) mixture, starting from [Cu₁₈H₁₆(DPPE)₆]²⁺ as the precursor. Details of syntheses are described in the Experimental Section and in Scheme 1. Following the earlier report by Li et al., the precursor cluster was prepared by reducing the Cu-DPPE precursor.⁵² The essential characterization of the [Cu₁₈H₁₆(DPPE)₆]²⁺ cluster, including UV-vis and MS data, is summarized in Figure S1. After a one-pot synthesis, Cu₄ and Cu₆ clusters were separated efficiently through selective crystallization. The Cu₄ NC was crystallized as transparent rhombus-shaped single crystals upon hexane vapor diffusion into a DCM/DMF mixture at 4 °C. In contrast, the Cu₆ NC was crystallized as yellow hexagonal crystals via slow evaporation of the reaction mixture at the same temperature. These crystals were soluble in DMF and ACN. The as-grown single crystals of Cu₄ exhibited intense green emission, while Cu₆ crystals exhibited bright red luminescence under a ~365 nm UV lamp.

Single-Crystal Structures. The molecular structures of the clusters were determined by SC-XRD. An optical microscopic image of the rhombus-shaped Cu₄ crystals is shown in Figure 1a. The FESEM micrograph further verified the morphology of the crystals, and the EDS elemental mapping shows the presence of Cu, S, N, O, and P in the atomic weight percentages of 26.03, 12.75, 9.56, 13.63, and 7.01, respectively (shown in Figure S3e). SC-XRD revealed that Cu₄ was crystallized in an orthorhombic crystal system with the space group of Pna2₁, having a cell volume of 5971.4 Å³ (Table S1). The structure of the cluster, including ligands, is presented in Figure 1c. This cluster comprises a Cu₄S₂ core protected by two mercaptionic acid ligands and phosphines. Two dimeric (Cu₂) units are connected through bridging S atoms, with Cu–S distances ranging from 2.211 to 2.937 Å. For these Cu₂ units, one Cu center is tetra-coordinated (one μ₃-S, one P, one O, and one Cu), while the other Cu is penta-coordinated (two μ₃-S, one P, one N, and one Cu). The Cu–Cu distances are in the range of 2.75–2.81 Å, revealing intermetallic cuprophilic interactions. Each DPPE

ligand is connected with the Cu₂ unit through the P-end, covering Cu–P distances of 2.170–2.221 Å. The MNA ligand is connected to the Cu₄S₂ core through N and O atoms, where the C–N bond distances are 2.016 and 2.026 Å and the Cu–O bond distances are 1.917 and 1.981 Å, respectively. Four molecules of the Cu₄ cluster are presented in the unit cell (Figure S4a). Single crystals of the Cu₆ cluster were hexagonal (Figure 1b). The FESEM micrograph shows the surface morphology of the crystals, and the EDS elemental mapping confirms the presence of elements Cu, S, N, and O with atomic percentages of 34.58, 18.29, 5.29, and 10.26, respectively (shown in the inset of Figure S3f). SC-XRD reveals that Cu₆ was crystallized in a triclinic crystal system with the space group of P-1, having a cell volume of 1923.8 Å³ (Table S3). The asymmetric unit of the Cu₆ NC is Cu₃(MNA-H)_{3.5} DMF, as one of the DMF molecules is disordered around the inversion center. This cluster is composed of a Cu₆S₆ core, where two Cu₃S₃ chair-like geometries are interconnected by Cu–Cu bonds, and it is protected by six 2-mercaptionic acids (shown in Figure S4b). The Cu–Cu bond distances in each Cu₃ unit are 2.696 and 2.765 Å, respectively, while the Cu–S and Cu–N bond distances are 2.223–2.269 and 2.023–2.058 Å, respectively (Figure S4d). One molecule was present in each unit cell (Figure S4b). The extended structural packing of Cu₆ showed that the DMF molecules are entrapped in the lattice, forming H-bonds with mercaptionic acid ligands (Figure S5b).

Other Characterizations. The molecular composition of the clusters was analyzed through high-resolution mass spectrometric studies using a Waters Synapt G2Si HDMS instrument. Instrumental details and ionization conditions are mentioned in the characterization part of the manuscript. The Cu₄ NC was ionized in positive ion mode with a characteristic peak at *m/z* 1357.95 (1+), which corresponds to [Cu₄(MNA)₂(DPPE)₂]⁺. The experimental and theoretical isotopic distributions agreed well (shown in Figure 2a, left inset). Other prominent mass peaks observed at *m/z* 1380.90 (1+), 1396.94 (1+), and 1434.92 (1+) (marked as i, ii, and iii, respectively) are attributed to sodium and potassium species attached to the molecular ion of the cluster (Figure S7a,b). Collision-energy (CE)-dependent fragmentation provides further structural insight into the molecular species. Upon increase in CE, another peak at *m/z* 960.28 was observed,

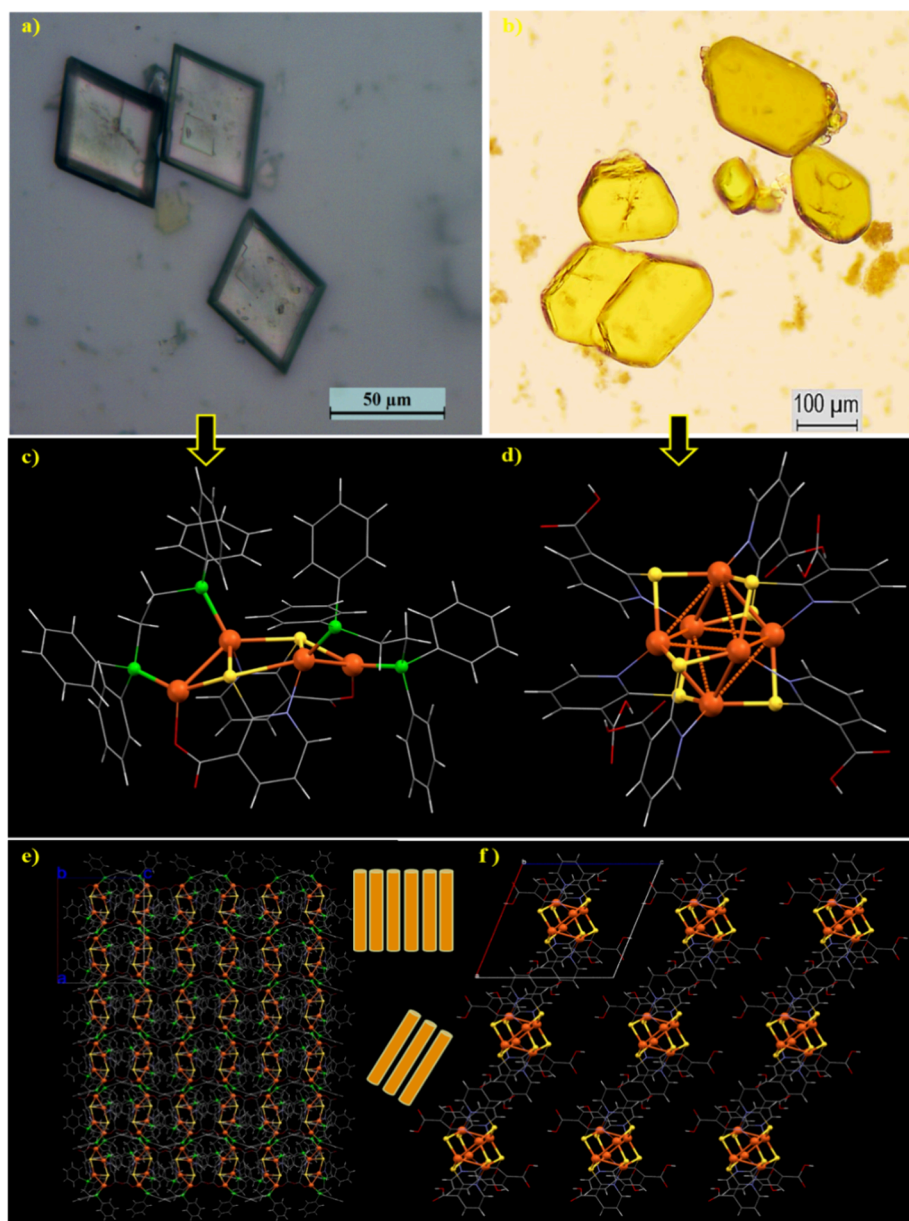


Figure 1. Optical microscopic images of the crystals of (a) Cu_4 and (b) Cu_6 NCs. Single-crystal structures of individual (c) Cu_4 and (d) Cu_6 (DMF molecules in the Cu_6 NC are removed for clarity). Structured packing ($3 \times 3 \times 3$ along the b -axis) of (e) Cu_4 and (f) Cu_6 NCs, respectively. Atomic color code: orange = Cu, yellow = S, green = P, gray = C, red = O, blue = N, and white = H.

which was assigned as $[\text{Cu}_4(\text{MNA})_2(\text{DPPE})]^+$. This species underwent a sequential loss of 44 mass units (due to CO_2 losses) upon increase in CE, resulting in species at m/z 916.14 and 872.38, respectively. Another species $[\text{Cu}_2(\text{MNA})(\text{DPPE})]^+$ at $m/z = 678.95$ was observed as a product of symmetrical dissociation, where the parent molecule underwent a specific fragmentation that led to this new species. Loss of CO_2 yielded another species at $m/z = 635.16$. On the other hand, Cu_6 was ionized in negative ion mode. The molecular ion peak was observed at m/z 1305.25 (1^-), which corresponds to $[\text{Cu}_6(\text{MNA-H})_5(\text{MNA})]^-$. Experimental and theoretical mass spectra match well (shown in the right inset of Figure 3a). One MNA-H ligand loss yielded the peak at m/z 1151.12 (1^-), which corresponds to $[\text{Cu}_6(\text{MNA-H})_4(\text{MNA})]^-$ (Figure 3a). A further increase in CE to the molecular ion peak yielded a loss of two ligands, and the peaks at m/z 1151.12 (1^-) and m/z 996.12 were observed. The

peak at m/z 996.12 corresponds to $[\text{Cu}_6(\text{MNA-H})_3(\text{MNA})]^-$. Sequential loss of 44 mass units from this species was observed (shown in Figure 3b). The other fragmented species was at m/z 715.64, which corresponds to $[\text{Cu}_3(\text{MNA-H})_2(\text{MNA})]^-$. Sequential loss of three $-\text{CO}_2$ molecules yielded three other species (shown in Figure 3b). The other fragmented species was at m/z 715.64, which corresponds to $[\text{Cu}_3(\text{MNA-H})_2(\text{MNA})]^-$. Sequential loss of three $-\text{CO}_2$ molecules yielded other three species (shown in Figure 3b). The UV-vis absorption spectrum of the Cu_4 NC cluster in acetonitrile shows peaks at 296 and 385 nm, revealing a characteristic pattern indicating its molecular nature (Figure S2a). The Cu_6 NC in acetonitrile exhibits UV-vis absorption features at 207, 238, 300, and 382 nm (Figure S2b). Time-dependent UV-vis spectra indicate the structural stability of the cluster for up to 20 days (Figure S2). Comparative FT-IR studies were performed to understand the binding of ligands to the

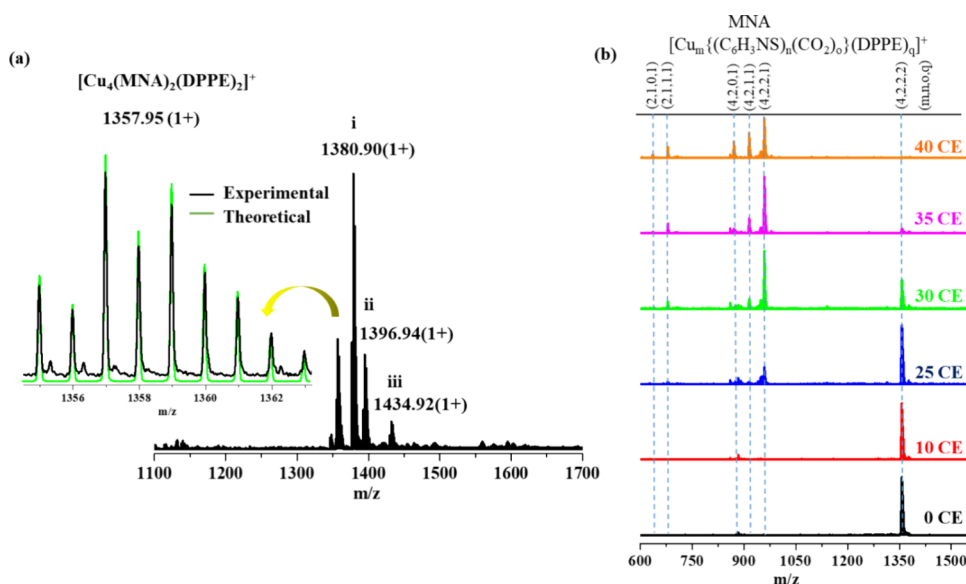


Figure 2. (a) Full-range high-resolution ESI MS spectrum of Cu_4 in positive ion mode; the left inset shows the isotopic mass distribution of theoretical and experimental spectra. (b) CE-dependent MS/MS fragmentation pattern of the molecular ion peak at m/z 1357.95 (1+).

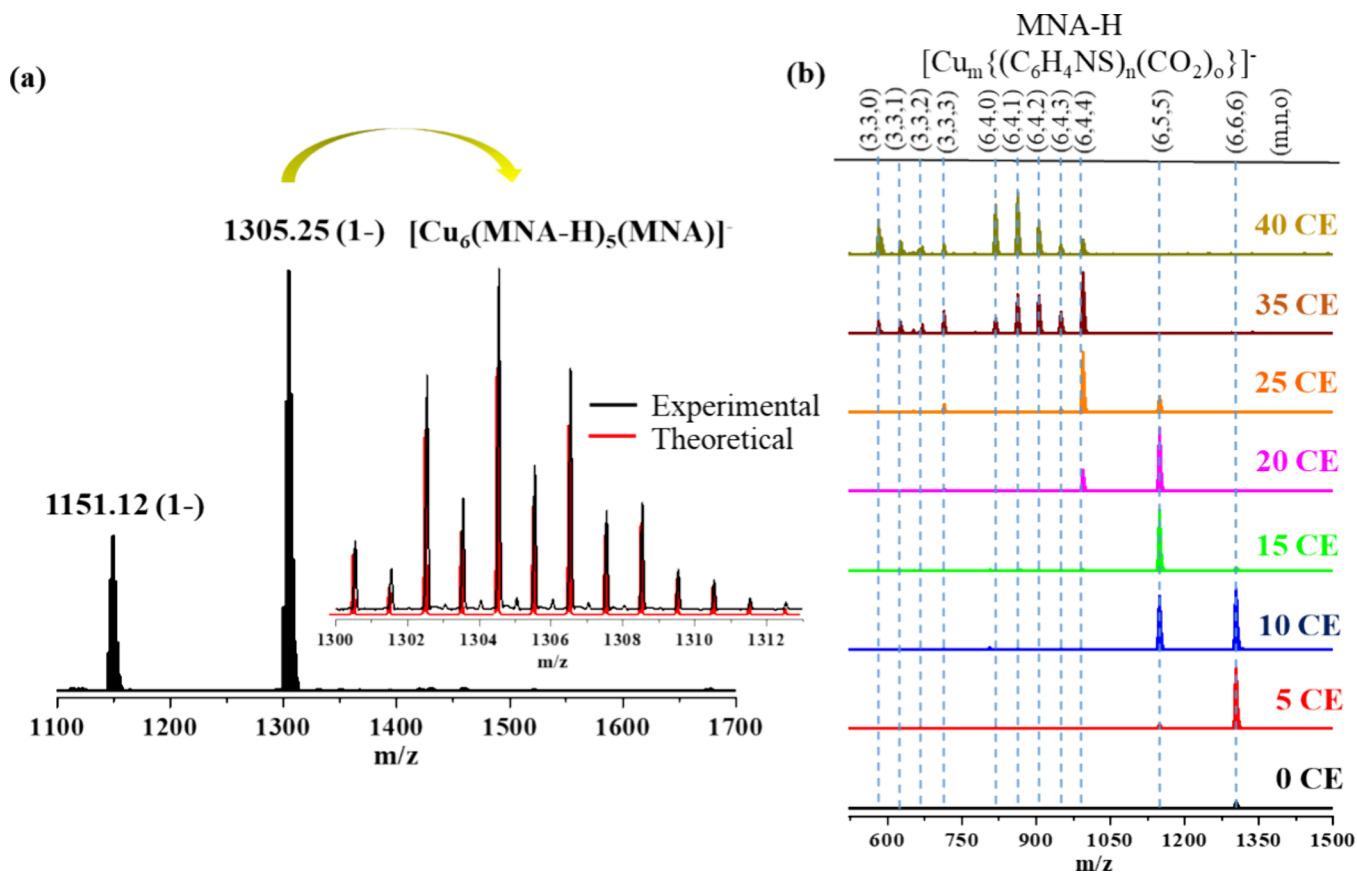


Figure 3. (a) Full range high-resolution ESI MS spectrum of the Cu_6 NC in negative ion mode; the right inset shows the isotopic mass distribution of theoretical and experimental spectra. (b) CE-dependent MS/MS fragmentation pattern of the molecular ion peak at m/z 1305.25 (1-).

molecular structure of Cu_4 and Cu_6 NCs. A strong vibrational peak at 1605 cm^{-1} corresponds to the $-\text{COO}$ vibration of the bound mercapto acid group in the Cu_4 NC. Another prominent peak at 577 cm^{-1} is due to the $\text{Cu}-\text{S}$ stretching mode (Figure S8). Besides, moderately intense peaks at 1093, 1435, and 1380 cm^{-1} were observed due to $\text{C}-\text{O}$, $\text{C}=\text{C}$, and $\text{C}=\text{N}$ stretching, respectively. The Cu_6 NC also shows a

similar type of spectrum except for two kinds of $-\text{COOH}$ stretching (Figure S9): one peak at 1696 cm^{-1} (uncoordinated $-\text{COOH}$) and the other peak at 1390 cm^{-1} ($-\text{COO}$ bonded to Cu). The XPS spectra of Cu_4 and Cu_6 show the oxidation state of the elements present in the cluster (Figures S10 and S11). In the Cu_4 NC, the Cu 2p region shows $2p_{3/2}$ and $2p_{1/2}$ features at 930.9 and 950.8 eV (Figure S10b), respectively, and

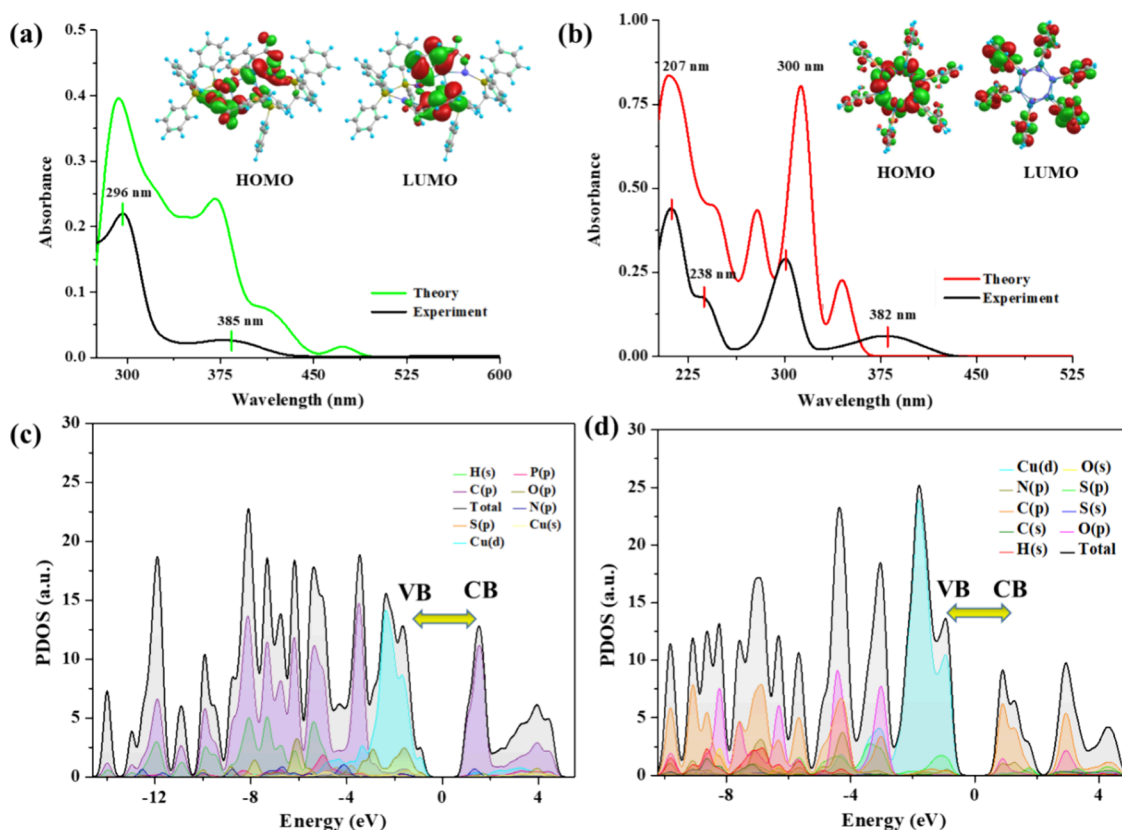


Figure 4. (a, b) Correlation between experimental absorption spectra (sample in acetonitrile solvent) and theoretical spectra (in solvent medium) of Cu_4 and Cu_6 NCs; the insets show the HOMO and LUMO of the respective clusters. (c, d) PDOS spectra of Cu_4 and Cu_6 NCs with respect to individual atomic orbitals (VB, valence band and CB, conduction band).

the absence of the satellite peak suggests the metal-like zero oxidation state for Cu. The XPS spectrum of Cu_6 follows a similar pattern (Figure S11). The presence of other elements is also verified in the XPS analysis (Figures S10 and S11). Thermogravimetric analysis (TGA) and DTG measurements showed thermal stability of Cu_4 and Cu_6 NCs up to 325 and 267 °C, respectively (Figures S22 and S23).

Theoretical Understanding of the Electronic Structure. Initially, both the clusters (Cu_4 and Cu_6) were optimized using the DFT method with the Gaussian 09 package,⁵³ and the optimized structures are shown in Figures S12a and S14a. Further computational details are provided in the Supporting Information. Using the optimized structures, electronic and optical spectra were analyzed. For the Cu_4 cluster, time-dependent DFT (TD-DFT) calculations in the presence of ACN solvent revealed two absorption peaks around 288 and 373 nm (Figure 4a), which closely resembled the experimentally observed bands. These peaks correspond to the transitions of HOMO−6 → LUMO + 20 (exp: 4.16 eV/296 nm) and HOMO−2 → LUMO + 7 (exp: 3.22 eV/385 nm), respectively. The theoretical calculations also showed two absorption bands in the low energy region around 408 and 468 nm, corresponding to the transitions of HOMO−2 → LUMO + 1 and HOMO → LUMO + 1, respectively. These transitions are shown in Figure S13a. Kohn–Sham (K–S) molecular orbital analysis indicated that the occupied MOs are composed of Cu(d), O(s-p), and S(s-p) orbitals (Figure S13b), while the unoccupied MOs are dominated by Cu(s-p), C(s-p), and N(s-p) orbitals. Electronic structures of the cluster were studied by conducting a projected density of states (PDOS) analysis using

the Vienna Ab initio Simulation Package and frontier molecular orbital analysis.^{54–56} The middle of the plots was set to zero to indicate the Fermi level. In this plot, orbitals with negative energy are considered to be HOMOs, and orbitals with positive energy are considered to be LUMOs. According to the PDOS analysis, the valence band of the Cu_4 NC consists predominantly of Cu(d), C(p), O(p), and H(s) states, and the conduction band is dominated by C(p) states (Figure 4c). The absorption peak of 385 nm is majorly due to metal-to-ligand transition (Figure S13). A TD-DFT calculation of the Cu_6 NC reveals four distinct optical absorption peaks (at 205, 240, 306, and 348 nm), which correspond to HOMO−25 → LUMO + 1 (5.99 eV/207 nm), HOMO−10 → LUMO + 11 (5.21 eV/238 nm), HOMO−8 → LUMO + 1 (4.13 eV, 300 nm), and HOMO−1 → LUMO + 4 (3.25 eV/382 nm) transitions, as shown in Figure S15a. The K–S analysis shows the dominance of core Cu(d) and S(s-p) orbitals in the occupied MOs, while unoccupied MOs are dominated by C(s-p) orbitals, as shown in Figure S15b. The PDOS analysis also agrees with the K–S analysis (Figure 4d). Therefore, the optical transitions take place mainly in the form of Cu-d (core) → C(s-p) (ligand) and S (s-p) (core) → C(s-p) (ligand).

Photoluminescence. The emission characteristics of Cu_4 and Cu_6 NCs were studied by photoluminescence spectroscopy. The NCs are nonemitting in solution (DMF and ACN), whereas bright luminescence appears in the solid crystalline state (Figures S16 and S17). The bulkiness of the ligands plays an essential role in decreasing the molecular motions, which helps to increase the radiative processes. Restriction of bond rotations and vibrations becomes more prominent in the solid

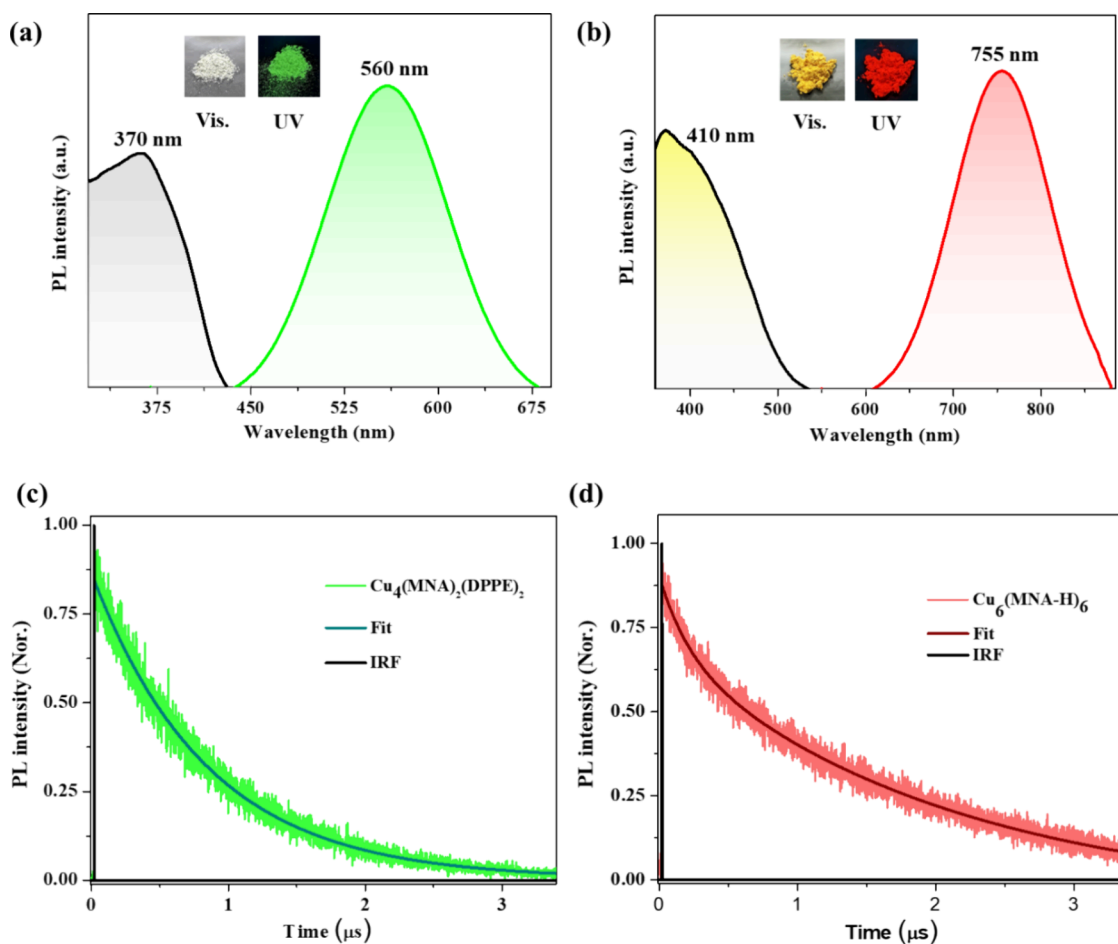


Figure 5. PL excitation and emission spectra of (a) Cu_4 and (b) Cu_6 NCs in the solid crystalline state. Insets show the photographs of respective clusters in microcrystalline powder form. Luminescence decay profiles of (c) Cu_4 and (d) Cu_6 NCs.

or well-ordered crystalline state due to strong intermolecular interactions (CH- π , CH-CH, and π - π), resulting in intense luminescence. A similar mechanism occurs for Cu_4 and Cu_6 NCs in their extended solid-state packing, which makes them emissive. In solution, molecules rotate freely and molecular vibrations dominate, which are responsible for quenching radiative paths. As a result, no luminescence was observed from the molecules in solution. Similarly, Cu clusters (Cu_4 and Cu_6) are nonluminescent in solution. Such an emission profile is reminiscent of several ultras-small Cu NCs.^{45,46} The Cu_4 NC shows emission maxima around 560 nm upon excitation at 370 nm. In comparison, Cu_6 emits at 755 nm at an excitation of 410 nm. Ligands in such small clusters play a role in charge transfer (ligand to metal charge transfer or vice versa).^{18,37–39} Emission lifetimes were measured to understand the role of excited states in luminescence. The Cu_4 NC exhibits a monoexponential decay lifetime of 0.84 μs (Figure 5c). On the other hand, the Cu_6 NC exhibits biexponential decay lifetime components of 205 ns and 2.04 μs with relative amplitudes of 22 and 78% (Figure 5d). Thus, the average lifetime of the Cu_6 NC was 1.64 μs . Upon oxygen exposure, the PL intensity for both the clusters was quenched, which indicates phosphorescence (Figures S18 and S19). Temperature-dependent luminescence from room temperature to 200 °C shows a gradual decrease in emission intensity (Figures S20 and S21). Using the integrating sphere method, we estimated the photoluminescence quantum efficiencies of 9.56 and 1.59%

for microcrystalline Cu_4 and Cu_6 NCs, respectively. For the Cu_4 NC, the calculated radiative decay rate constant (k_r) was $1.1 \times 10^5 \text{ s}^{-1}$ and the nonradiative decay rate constant (k_{nr}) was $1.2 \times 10^6 \text{ s}^{-1}$. On the other hand, for the Cu_6 NC, the calculated radiative decay rate constant (k_r) was $9.7 \times 10^3 \text{ s}^{-1}$ and the nonradiative decay rate constant (k_{nr}) was $6.1 \times 10^5 \text{ s}^{-1}$.

Mechanosensitive Luminescence. External stimuli such as temperature and pressure sometimes have an effect on the photophysical properties of luminescent materials. In this context, Cu-based materials with structure-specific luminescence are interesting (Table S5). Phosphine-protected luminescent Cu clusters with small nuclearities are sensitive to stimuli. This is reportedly due to the shortening of the Cu–Cu bond length upon applied pressure.^{49,50} In our work, Cu_4 and Cu_6 NCs exhibit “turn-off” luminescence upon ambient mechanical milling. Green (560 nm) and red emission (755 nm) of Cu_4 and Cu_6 are lost in the process, but solvent diffusion brings them back to the emissive state (Figure 6a,b). The applied force provides pressing and shearing along different directions of the molecular structure and disrupts the extended solid-state packing. As a result, the crushed and ground samples lose their well-ordered structure, accompanied by quenching of luminescence originating from tight packing (Figure S5). This type of transition was monitored by powder XRD. It revealed the phase change of the NC materials during mechanical milling and solvent vapor exposure (Figure 6e,f).

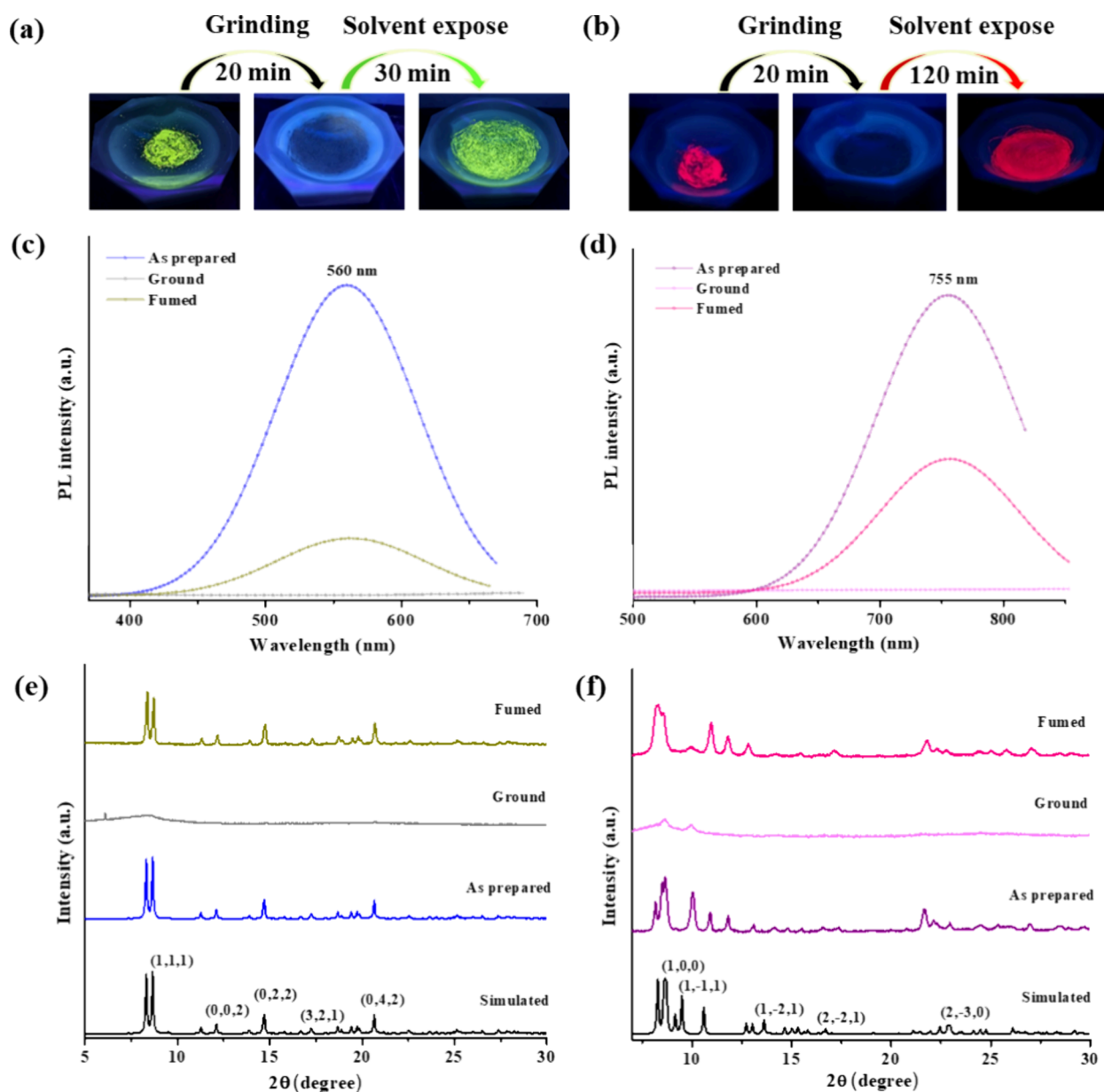


Figure 6. Mechanosensitive luminescence study. Photographic images of (a) Cu_4 and (b) Cu_6 NCs under 365 nm UV light. PL spectra of (c) Cu_4 and (d) Cu_6 NCs after ambient mechanical milling and vapor exposure. Comparative powder XRD patterns of microcrystalline (e) Cu_4 and (f) Cu_6 NCs.

Powder XRD peaks for both NCs match the theoretical data well, indicating the sample's crystalline purity. The ground NCs exhibit very few broad peaks in the powder XRD pattern, which reveals their nearly amorphous nature. PL was quenched for the ground sample. The reappearance of sharp diffraction peaks upon vapor diffusion shows reversible crystallinity induced by solvent molecules. The ground Cu_4 NC regains its emission within 30 min upon DCM vapor diffusion, whereas the Cu_6 NC takes around 120 min to regain emission by DMF vapor. The broadness of emission spectra is likely due to the materials' structural heterogeneity. Literature suggests that partial PL quenching is likely due to some permanent defects created when mechanical force is applied.⁵⁰ Roles of different solvents (volatile organic compounds and water) on luminescence recovery of the ground material were checked (Table S6). There were no significant changes in the emission wavelength in all of the cases. Polar solvents with H-bonding

ability play a crucial role in reverting the crystallinity and luminescence of the Cu_6 NC. It suggests the importance of noncovalent interactions between the ground NC and the solvent molecules.

CONCLUSIONS

This work presents the synthesis and characterization of a pair of luminescent mechanochromic Cu NCs. SC-XRD reveals flattened boat-like Cu_4S_2 and adamantane-like Cu_6S_6 kernel structures for Cu_4 and Cu_6 clusters, respectively. Both the nanomaterials show bright luminescence in their crystalline state, which relaxes in solution, making them nonemitting. The Cu_4 cluster shows green emission under exposure to UV light (365 nm), whereas Cu_6 shows red emission. The small cores of Cu_4S_2 and Cu_6S_6 are sensitive to mechanical milling, losing their luminescence but regaining it upon exposure to solvent vapors. The switchable mechanochromic luminescence ex-

hibited by these Cu NCs opens up possibilities for technologies such as strain sensing and chemical sensing. The ability to control luminescence through mechanical stimuli adds new attributes to such materials.

■ ASSOCIATED CONTENT

SI Supporting Information

The Supporting Information is available free of charge at <https://pubs.acs.org/doi/10.1021/acs.inorgchem.4c02617>.

Theoretical calculations, crystallographic information, UV–vis, FESEM, EDS, XPS, Fourier transform infrared, electronic transitions involving HOMO–LUMO, Kahn–Sham analysis, TG and DTG, and associated figures (PDF)

Accession Codes

CCDC numbers 2339995 and 2340002 contain the supplementary crystallographic data for this paper. These data can be obtained free of charge via www.ccdc.cam.ac.uk/data_request/cif, or by emailing data_request@ccdc.cam.ac.uk, or by contacting The Cambridge Crystallographic Data Centre, 12 Union Road, Cambridge CB2 1EZ, UK; fax: +44 1223 336033.

■ AUTHOR INFORMATION

Corresponding Authors

Biswarup Pathak – Department of Chemistry, Indian Institute of Technology Indore, Indore 453552, India; orcid.org/0000-0002-9972-9947; Email: biswarup@iiti.ac.in

Adarsh Kumaran Nair Valsala Devi – Department of Physics, Indian Institute of Science Education and Research Bhopal, Bhopal 462066, India; orcid.org/0000-0002-6337-6545; Email: adarsh@iiserb.ac.in

Thalappil Pradeep – DST Unit of Nanoscience (DST UNS) and Thematic Unit of Excellence (TUE), Department of Chemistry, Indian Institute of Technology, Madras, Chennai 600036, India; orcid.org/0000-0003-3174-534X; Email: pradeep@iitm.ac.in

Authors

Subrata Duary – DST Unit of Nanoscience (DST UNS) and Thematic Unit of Excellence (TUE), Department of Chemistry, Indian Institute of Technology, Madras, Chennai 600036, India

Arijit Jana – DST Unit of Nanoscience (DST UNS) and Thematic Unit of Excellence (TUE), Department of Chemistry, Indian Institute of Technology, Madras, Chennai 600036, India

Amitabha Das – Department of Chemistry, Indian Institute of Technology Indore, Indore 453552, India; orcid.org/0000-0002-5000-4451

Swetashree Acharya – DST Unit of Nanoscience (DST UNS) and Thematic Unit of Excellence (TUE), Department of Chemistry, Indian Institute of Technology, Madras, Chennai 600036, India

Amoghavarsha Ramachandra Kini – DST Unit of Nanoscience (DST UNS) and Thematic Unit of Excellence (TUE), Department of Chemistry, Indian Institute of Technology, Madras, Chennai 600036, India

Jayoti Roy – DST Unit of Nanoscience (DST UNS) and Thematic Unit of Excellence (TUE), Department of Chemistry, Indian Institute of Technology, Madras, Chennai 600036, India

Ajay Kumar Poonia – Department of Physics, Indian Institute of Science Education and Research Bhopal, Bhopal 462066, India; orcid.org/0000-0002-5551-7299

Deepak Kumar Patel – DST Unit of Nanoscience (DST UNS) and Thematic Unit of Excellence (TUE), Department of Chemistry, Indian Institute of Technology, Madras, Chennai 600036, India; orcid.org/0000-0003-2509-4165

Vivek Yadav – DST Unit of Nanoscience (DST UNS) and Thematic Unit of Excellence (TUE), Department of Chemistry, Indian Institute of Technology, Madras, Chennai 600036, India

P. K. Sudhadevi Antharjanam – Sophisticated Analytical Instrument Facility, Indian Institute of Technology Madras, Chennai 600036, India; orcid.org/0000-0002-8801-7530

Complete contact information is available at:

<https://pubs.acs.org/doi/10.1021/acs.inorgchem.4c02617>

Author Contributions

S.D. performed the synthesis, crystallization, and most of the experimental studies. A.J. helped SD for single-crystal measurements and gave inputs while writing the manuscript. A.D. performed theoretical calculations. B.P. was involved in the discussion of theoretical data. S.A. and J.R. performed the mass spectrometric studies. A.K.P. measured the PL lifetime of clusters. K.N.V.D.A. was involved in the discussion of the PL data. S.A. collected and analyzed the single-crystal data. D.K.P. and V.Y. were involved in discussions. A.R.K. performed XPS of the clusters. S.D. prepared all manuscript drafts. T.P. supervised the work and finalized the manuscript.

Notes

The authors declare no competing financial interest.

■ ACKNOWLEDGMENTS

S.D. acknowledges the Prime Minister's Research Fellowship (PMRF) from the Government of India (GoI). S.D. is thankful to the Sophisticated Analytical Instrument Facility, Indian Institute of Technology Madras (SAIF-IITM), for the SC-XRD and TG measurements. A.J. and J.R. acknowledge financial support from the IIT Madras. A.D. and A.R.K. thank the GoI for the UGC fellowships. S.A., D.K.P., and V.Y. are thankful for the PMRF grant. A.K.P. acknowledges the GoI for a CSIR fellowship. T.P. acknowledges funding from the Centre of Excellence (CoE) on Molecular Materials and Functions from the Institute of Eminence scheme of IIT Madras. K.N.V.D.A. and T. P. thank the Science and Engineering Research Board (SERB) for funding through the CRG/2019/002808 and SPR/2021/000439 research grants, respectively. T.P. thanks the Science and Engineering Research Board (SERB) for a J.C. Bose Fellowship.

■ REFERENCES

- (1) Chakraborty, I.; Pradeep, T. Atomically precise clusters of noble metals: emerging link between atoms and nanoparticles. *Chem. Rev.* **2017**, *117* (12), 8208–8271.
- (2) Jin, R.; Zeng, C.; Zhou, M.; Chen, Y. Atomically precise colloidal metal nanoclusters and nanoparticles: fundamentals and opportunities. *Chem. Rev.* **2016**, *116* (18), 10346–10413.
- (3) Jana, A.; Kini, A. R.; Pradeep, T. Atomically Precise Clusters: Chemical Evolution of Molecular Matter at the Nanoscale. *AsiaChemMag* **2023**, *3*, 56–65.

- (4) Pradeep, T., Ed. *Atomically Precise Metal Nanocluster*; Elsevier: Amsterdam, 2023; pp. 1–643.
- (5) Chakraborty, P.; Nag, A.; Chakraborty, A.; Pradeep, T. Approaching materials with atomic precision using supramolecular cluster assemblies. *Acc. Chem. Res.* **2019**, *52* (1), 2–11.
- (6) Kang, X.; Zhu, M. Tailoring the photoluminescence of atomically precise nanoclusters. *Chem. Soc. Rev.* **2019**, *48* (8), 2422–2457.
- (7) Yang, S.; Zhu, M. Insight of the photoluminescence of atomically precise bimetallic nanoclusters with free electrons. *J. Chin. Chem. Soc.* **2020**, *67* (12), 2171–2181.
- (8) Xie, Y. P.; Shen, Y. L.; Duan, G. X.; Han, J.; Zhang, L. P.; Lu, X. Silver nanoclusters: synthesis, structures and photoluminescence. *Mater. Chem. Front.* **2020**, *4* (8), 2205–2222.
- (9) AbdulHalim, L. G.; Bootharaju, M. S.; Tang, Q.; Del Gobbo, S.; AbdulHalim, R. G.; Eddaoudi, M.; Jiang, D. E.; Bakr, O. M. Ag₂₉(BDT)₁₂(TPP)₄: a tetravalent nanocluster. *J. Am. Chem. Soc.* **2015**, *137* (37), 11970–11975.
- (10) Jana, A.; Chakraborty, P.; Dar, W. A.; Chandra, S.; Khatun, E.; Kannan, M. P.; Ras, R. H.; Pradeep, T. Dual emitting Ag₃₅ nanocluster protected by 2-pyrene imine thiol. *Chem. Commun.* **2020**, *56* (83), 12550–12553.
- (11) (a) Shen, H.; Wang, L.; López-Estrada, O.; Hu, C.; Wu, Q.; Cao, D.; Malola, S.; Teo, B. K.; Häkkinen, H.; Zheng, N. Copper-hydride nanoclusters with enhanced stability by N-heterocyclic carbenes. *Nano Res.* **2021**, *14*, 3303–3308. (b) Shen, H.; Wu, Q.; Malola, S.; Han, Y. Z.; Xu, Z.; Qin, R.; Tang, X.; Chen, Y. B.; Teo, B. K.; Häkkinen, H.; Zheng, N. N-heterocyclic carbene-stabilized gold nanoclusters with organometallic motifs for promoting catalysis. *J. Am. Chem. Soc.* **2022**, *144* (24), 10844–10853.
- (12) Maity, P.; Takano, S.; Yamazoe, S.; Wakabayashi, T.; Tsukuda, T. Binding motif of terminal alkynes on gold clusters. *J. Am. Chem. Soc.* **2013**, *135* (25), 9450–9457.
- (13) McCandler, C. A.; Dahl, J. C.; Persson, K. A. Phosphine-Stabilized Hidden Ground States in Gold Clusters Investigated via a Au_n(PH₃)_m Database. *ACS Nano* **2023**, *17* (2), 1012–1021.
- (14) Liu, K. G.; Gao, X. M.; Liu, T.; Hu, M. L.; Jiang, D. E. All-carboxylate-protected superatomic silver nanocluster with an unprecedented rhombohedral Ag₈ core. *J. Am. Chem. Soc.* **2020**, *142* (40), 16905–16909.
- (15) (a) Yang, H.; Wang, Y.; Huang, H.; Gell, L.; Lehtovaara, L.; Malola, S.; Häkkinen, H.; Zheng, N. All-thiol-stabilized Ag₄₄ and Au₁₂Ag₃₂ nanoparticles with single-crystal structures. *Nat. Commun.* **2013**, *4* (1), 2422. (b) Joshi, C. P.; Bootharaju, M. S.; Alhilaly, M. J.; Bakr, O. M. [Ag₂₅(SR)₁₈][−]: The “golden” silver nanoparticle. *J. Am. Chem. Soc.* **2015**, *137* (36), 11578–11581. (c) Jana, A.; Unnikrishnan, P. M.; Poonia, A. K.; Roy, J.; Jash, M.; Paramasivam, G.; Machacek, J.; Adarsh, K. N. V. D.; Base, T.; Pradeep, T. Carboranethiol-Protected Propeller-Shaped Photoresponsive Silver Nanomolecule. *Inorg. Chem.* **2022**, *61* (23), 8593–8603.
- (16) (a) Heaven, M. W.; Dass, A.; White, P. S.; Holt, K. M.; Murray, R. W. Crystal structure of the gold nanoparticle [N(C₈H₁₇)₄][Au₂₅(SCH₂CH₂Ph)₁₈]. *J. Am. Chem. Soc.* **2008**, *130* (12), 3754–3755. (b) Chen, T.; Lin, H.; Cao, Y.; Yao, Q.; Xie, J. Interactions of metal nanoclusters with light: fundamentals and applications. *Adv. Mater.* **2022**, *34* (25), No. 2103918. (c) Jadzinsky, P. D.; Calero, G.; Ackerson, C. J.; Bushnell, D. A.; Kornberg, R. D. Structure of a thiol monolayer-protected gold nanoparticle at 1.1 Å resolution. *Science* **2007**, *318* (5849), 430–433.
- (17) Häkkinen, H. Atomic and electronic structure of gold clusters: understanding flakes, cages and superatoms from simple concepts. *Chem. Soc. Rev.* **2008**, *37* (9), 1847–1859.
- (18) Wang, J. J.; Chen, C.; Chen, W. G.; Yao, J. S.; Yang, J. N.; Wang, K. H.; Yin, Y. C.; Yao, M. M.; Feng, L. Z.; Ma, C.; Fan, F. J. Highly luminescent copper iodide cluster-based inks with photoluminescence quantum efficiency exceeding 98%. *J. Am. Chem. Soc.* **2020**, *142* (8), 3686–3690.
- (19) Zhang, J.; Zhang, L.; Cai, P.; Xue, X.; Wang, M.; Zhang, J.; Tu, G. Enhancing stability of red perovskite nanocrystals through copper substitution for efficient light-emitting diodes. *Nano Energy* **2019**, *62*, 434–441.
- (20) Wei, W.; Lu, Y.; Chen, W.; Chen, S. One-pot synthesis, photoluminescence, and electrocatalytic properties of subnanometer-sized copper clusters. *J. Am. Chem. Soc.* **2021**, *133* (7), 2060–2063.
- (21) (a) Liu, L. J.; Wang, Z. Y.; Wang, Z. Y.; Wang, R.; Zang, S. Q.; Mak, T. C. Mediating CO₂ electroreduction activity and selectivity over atomically precise copper clusters. *Angew. Chem., Int. Ed.* **2022**, *134* (35), No. e202205626. (b) Xu, H.; Rebollar, D.; He, H.; Chong, L.; Liu, Y.; Liu, C.; Sun, C. J.; Li, T.; Muntean, J. V.; Winans, R. E.; Liu, D. J. Highly selective electrocatalytic CO₂ reduction to ethanol by metallic clusters dynamically formed from atomically dispersed copper. *Nat. Energy* **2020**, *5* (8), 623–632.
- (22) Wang, Y. M.; Lin, X. C.; Mo, K. M.; Xie, M.; Huang, Y. L.; Ning, G. H.; Li, D. An Atomically Precise Pyrazolate-Protected Copper Nanocluster Exhibiting Exceptional Stability and Catalytic Activity. *Angew. Chem., Int. Ed.* **2023**, *62* (9), No. e202218369.
- (23) (a) Das, A. K.; Biswas, S.; Wani, V. S.; Nair, A. S.; Pathak, B.; Mandal, S. [Cu₁₈H₃(S-Adm)₁₂(PPh₃)₄Cl₂]: fusion of Platonic and Johnson solids through a Cu (0) center and its photophysical properties. *Chem. Sci.* **2022**, *13* (25), 7616–7625. (b) Cook, A. W.; Jones, Z. R.; Wu, G.; Scott, S. L.; Hayton, T. W. An organometallic Cu₂₀ nanocluster: Synthesis, characterization, immobilization on silica, and “Click” chemistry. *J. Am. Chem. Soc.* **2018**, *140* (1), 394–400.
- (24) (a) Das, A. K.; Biswas, S.; Pal, A.; Manna, S. S.; Sardar, A.; Mondal, P. K.; Sahoo, B.; Pathak, B.; Mandal, S. A thiolated copper-hydride nanocluster with chloride bridging as a catalyst for carbonylative C–N coupling of aryl amines under mild conditions: a combined experimental and theoretical study. *Nanoscale* **2024**, *16* (7), 3583–3590. (b) Zhang, L. M.; Mak, T. C. Comproportionation synthesis of copper (I) alkynyl complexes encapsulating polyoxomolybdate templates: bowl-shaped Cu₃₃ and peanut-shaped Cu₆₂ nanoclusters. *J. Am. Chem. Soc.* **2016**, *138* (9), 2909–2912.
- (25) (a) Biswas, S.; Hossain, S.; Kosaka, T.; Sakai, J.; Arima, D.; Niihori, Y.; Mitsui, M.; Jiang, D. E.; Das, S.; Wang, S.; Negishi, Y. Nested Keplerian architecture of [Cu₅₈H₂₀(SPR)₃₆(PPh₃)₈]²⁺ nanoclusters. *Chem. Commun.* **2023**, *59* (61), 9336–9339. (b) Huang, R. W.; Yin, J.; Dong, C.; Ghosh, A.; Alhilaly, M. J.; Dong, X.; Hedhili, M. N.; Abou-Hamad, E.; Alamer, B.; Nematulloev, S.; Han, Y. [Cu₈₁(PhS)₄₆(tBuNH₂)₁₀(H)₃₂]³⁺ reveals the coexistence of large planar cores and hemispherical shells in high-nuclearity copper nanoclusters. *J. Am. Chem. Soc.* **2020**, *142* (19), 8696–8705.
- (26) Fu, M. L.; Issac, I.; Fenske, D.; Fuhr, O. Metal-Rich Copper Chalcogenide Clusters at the Border Between Molecule and Bulk Phase: The Structures of [Cu₉₃Se₄₂(SeC₆H₄SMe)₉(PPh₃)₁₈], [Cu₉₆Se₄₅(SeC₆H₄SMe)₆(PPh₃)₁₈], and [Cu₁₃₆S₅₆(SCH₂C₄H₃O)₂₄(dpppt)₁₀]. *Angew. Chem., Int. Ed.* **2010**, *49* (38), 6899–6903.
- (27) Baghdasaryan, A.; Besnard, C.; Lawson Daku, L. M.; Delgado, T.; Burgi, T. Thiolato protected copper sulfide cluster with the tentative composition Cu₇₄S₁₅(2-PET)₄₅. *Inorg. Chem.* **2020**, *59* (4), 2200–2208.
- (28) Huang, Q. Q.; Hu, M. Y.; Li, Y. L.; Chen, N. N.; Li, Y.; Wei, Q. H.; Fu, F. Novel ultrabright luminescent copper nanoclusters and application in light-emitting devices. *Chem. Commun.* **2021**, *57* (77), 9890–9893.
- (29) Oлару, M.; Rychagova, E.; Ketkov, S.; Shynkarenko, Y.; Yakunin, S.; Kovalenko, M. V.; Yablonskiy, A.; Andreev, B.; Kleemiss, F.; Beckmann, J.; Vogt, M. A small cationic organo-copper cluster as thermally robust highly photo- and electroluminescent material. *J. Am. Chem. Soc.* **2020**, *142* (1), 373–381.
- (30) (a) Huang, R. W.; Song, X.; Chen, S.; Yin, J.; Maity, P.; Wang, J.; Shao, B.; Zhu, H.; Dong, C.; Yuan, P.; Ahmad, T. Radioluminescent Cu–Au Metal Nanoclusters: Synthesis and Self-Assembly for Efficient X-ray Scintillation and Imaging. *J. Am. Chem. Soc.* **2023**, *145* (25), 13816–13827. (b) Kiracki, K.; Fejfarová, K.; Martincik, J.; Nikl, M.; Lang, K. Tetranuclear copper (I) iodide complexes: a new class of X-ray phosphors. *Inorg. Chem.* **2017**, *56* (8), 4609–4614.

- (31) Das, N. K.; Ghosh, S.; Priya, A.; Datta, S.; Mukherjee, S. Luminescent copper nanoclusters as a specific cell-imaging probe and a selective metal ion sensor. *J. Phys. Chem. C* **2015**, *119* (43), 24657–24664.
- (32) Jana, A.; Spoorthi, B. K.; Nair, A. S.; Nagar, A.; Pathak, B.; Base, T.; Pradeep, T. A luminescent Cu₄ cluster film grown by electrospray deposition: a nitroaromatic vapour sensor. *Nanoscale* **2023**, *15* (18), 8141–8147.
- (33) Rival, J. V.; Mymoona, P.; Vinoth, R.; Mohan, A. V.; Shibu, E. S. Light-emitting atomically precise nanocluster-based flexible QR codes for anticounterfeiting. *ACS Appl. Mater. Interfaces* **2021**, *13* (8), 10583–10593.
- (34) Nasrollahpour, H.; Sánchez, B. J.; Sillanpää, M.; Moradi, R. Metal nanoclusters in point-of-care sensing and biosensing applications. *ACS Appl. Nano Mater.* **2023**, *6* (14), 12609–12672.
- (35) Jana, A.; Jash, M.; Dar, W. A.; Roy, J.; Chakraborty, P.; Paramasivam, G.; Lebedkin, S.; Kirakci, K.; Manna; Antharjanam, S.; Machacek, J.; Kucerakova, M.; Ghosh, S.; Lang, K.; Kappes, M. M.; Base, T.; Pradeep, T. Carborane-thiol protected copper nanoclusters: stimuli-responsive materials with tunable phosphorescence. *Chem. Sci.* **2023**, *14* (6), 1613–1626.
- (36) Biswas, S.; Negishi, Y. A Comprehensive Analysis of Luminescent Crystallized Cu Nanoclusters. *J. Phys. Chem. Lett.* **2024**, *15* (4), 947–958.
- (37) Yang, T. Q.; Peng, B.; Shan, B. Q.; Zong, Y. X.; Jiang, J. G.; Wu, P.; Zhang, K. Origin of the photoluminescence of metal nanoclusters: from metal-centered emission to ligand-centered emission. *Nanomater.* **2020**, *10* (2), 261.
- (38) Zhu, C.; Xin, J.; Li, J.; Li, H.; Kang, X.; Pei, Y.; Zhu, M. Fluorescence or phosphorescence? The metallic composition of the nanocluster kernel does matter. *Angew. Chem. Int. Ed.* **2022**, *134* (31), No. e202205947.
- (39) (a) Singh, N.; Raul, K. P.; Poulouse, A.; Mughesh, G.; Venkatesh, V. Highly stable pyrimidine based luminescent copper nanoclusters with superoxide dismutase mimetic and nitric oxide releasing activity. *ACS Appl. Bio Mater.* **2020**, *3* (11), 7454–7461. (b) Wang, Z.; Zhang, S.; Xie, H.; Zhang, N.; Wang, W.; Li, S.; Xin, X. Dispersing hydrophobic copper nanoclusters in aqueous solutions triggered by polyoxometalate with aggregation-induced emission properties. *Colloids Surf. A Physicochem. Eng. Asp.* **2023**, *664*, No. 131147. (c) Li, Y.; Feng, L.; Yan, W.; Hussain, I.; Su, L.; Tan, B. PVP-templated highly luminescent copper nanoclusters for sensing trinitrophenol and living cell imaging. *Nanoscale* **2019**, *11* (3), 1286–1294. (c) Dong, G.; Pan, Z.; Han, B.; Tao, Y.; Chen, X.; Luo, G. G.; Sun, P.; Sun, C.; Sun, D. Multi-layer 3D Chirality and Double-Helical Assembly in a Copper Nanocluster with a Triple-Helical Cu₁₅ Core. *Angew. Chem., Int. Ed.* **2023**, *62* (24), No. e202302595.
- (40) Ai, Y.; Li, Y.; Chan, M. H. Y.; Xiao, G.; Zou, B.; Yam, V. W. W. Realization of distinct mechano- and piezochromic behaviors via alkoxy chain length-modulated phosphorescent properties and multidimensional self-assembly structures of dinuclear platinum (II) complexes. *J. Am. Chem. Soc.* **2021**, *143* (28), 10659–10667.
- (41) Chen, T.; Yang, S.; Chai, J.; Song, Y.; Fan, J.; Rao, B.; Sheng, H.; Yu, H.; Zhu, M. Crystallization-induced-emission enhancement: A novel fluorescent Au-Ag bimetallic nanocluster with precise atomic structure. *Sci. Adv.* **2017**, *3* (8), No. e1700956.
- (42) Crocker, R. D.; Pace, D. P.; Zhang, B.; Lyons, D. J.; Bhadbhade, M. M.; Wong, W. W.; Mai, B. K.; Nguyen, T. V. Unusual alternating crystallization-induced emission enhancement behavior in non-conjugated ω -phenylalkyltropylium salts. *J. Am. Chem. Soc.* **2021**, *143* (48), 20384–20394.
- (43) Mei, J.; Leung, N. L.; Kwok, R. T.; Lam, J. W.; Tang, B. Z. Aggregation-induced emission: together we shine, united we soar! *Chem. Rev.* **2015**, *115* (21), 11718–11940.
- (44) Shi, Y. E.; Ma, J.; Feng, A.; Wang, Z.; Rogach, A. L. Aggregation-induced emission of copper nanoclusters. *Aggregate* **2021**, *2* (6), 112.
- (45) Kitagawa, H.; Ozawa, Y.; Toriumi, K. Flexibility of cubane-like Cu₄I₄ framework: temperature dependence of molecular structure and luminescence thermochromism of [Cu₄I₄(PPh₃)₄] in two polymorphic crystalline states. *Chem. Commun.* **2010**, *46* (34), 6302–6304.
- (46) Yuan, J.; Wang, L.; Wang, Y.; Hao, J. Stimuli-Responsive Fluorescent Nanoswitches: Solvent-Induced Emission Enhancement of Copper Nanoclusters. *Chem.—Eur. J.* **2020**, *26* (16), 3545–3554.
- (47) Perruchas, S.; Le Goff, X. F.; Maron, S.; Maurin, I.; Guillen, F.; Garcia, A.; Gacoin, T.; Boilot, J. P. Mechanochromic and thermochromic luminescence of a copper iodide cluster. *J. Am. Chem. Soc.* **2010**, *132* (32), 10967–10969.
- (48) Benito, Q.; Le Goff, X. F.; Maron, S.; Fargues, A.; Garcia, A.; Martineau, C.; Taulelle, F.; Kahlal, S.; Gacoin, T.; Boilot, J. P.; Perruchas, S. Polymorphic copper iodide clusters: insights into the mechanochromic luminescence properties. *J. Am. Chem. Soc.* **2014**, *136* (32), 11311–11320.
- (49) Huitorel, B.; Utrera-Melero, R.; Massuyeau, F.; Mevelec, J. Y.; Baptiste, B.; Polian, A.; Gacoin, T.; Martineau-Corcoss, C.; Perruchas, S. Luminescence mechanochromism of copper iodide clusters: a rational investigation. *Dalton Trans.* **2019**, *48* (22), 7899–7909.
- (50) Utrera-Melero, R.; Huitorel, B.; Cordier, M.; Massuyeau, F.; Mevellec, J. Y.; Stephant, N.; Deniard, P.; Latouche, C.; Martineau-Corcoss, C.; Perruchas, S. Mechanically responsive luminescent films based on copper iodide clusters. *J. Mater. Chem. C* **2021**, *9* (25), 7991–8001.
- (51) Shi, P.; Deng, D.; He, C.; Ji, L.; Duan, Y.; Han, T.; Suo, B.; Zou, W. Mechanochromic luminescent materials with aggregation-induced emission: mechanism study and application for pressure measuring and mechanical printing. *Dyes and Pigment.* **2020**, *173*, No. 107884.
- (52) Li, J.; Ma, H. Z.; Reid, G. E.; Edwards, A. J.; Hong, Y.; White, J. M.; Mulder, R. J.; O'Hair, R. A. Synthesis and X-Ray Crystallographic Characterization of Frustum-Shaped Ligated [Cu₁₈H₁₆(DPPPE)₆]²⁺ and [Cu₁₆H₁₄(DPPA)₆]²⁺ Nanoclusters and Studies on Their H₂ Evolution Reactions. *Chem.—Eur. J.* **2018**, *24* (9), 2070–2074.
- (53) Frisch, M. J.; Trucks, G. W.; Schlegel, H. B.; Scuseria, G. E.; Robb, M. A.; Cheeseman, J. R.; Scalmani, G.; Barone, V.; Mennucci, B.; Petersson, G. A. et al. *Gaussian 09, Revision B.01*; Gaussian Inc.: Wallingford, CT, 2009.
- (54) Blöchl, P. E. Projector augmented-wave method. *Phys. Rev. B* **1994**, *50* (24), 17953.
- (55) Kresse, G.; Joubert, D. From ultrasoft pseudopotentials to the projector augmented-wave method. *Phys. Rev. B* **1999**, *59* (3), 1758.
- (56) Kresse, G.; Furthmüller, J. Efficient iterative schemes for ab initio total-energy calculation using a plane-wave basis set. *Phys. Rev. B* **1996**, *54* (16), 11169.